Research Article | Vol. 27, No. 5 | 4 Mar 2019 | OPTICS EXPRESS 6495
Optics EXPRESS

Towards subterahertz bandwidth ultracompact lithium niobate electrooptic modulators

AMIRMAHDI HONARDOOST,[1,2] FARZANEH ARAB JUNEGHANI,[3] REZA SAFIAN,[4] AND SASAN FATHPOUR[1,2,*]

[1] *CREOL, The College of Optics and Photonics, University of Central Florida, Orlando, FL 32816, USA*
[2] *Department of Electrical and Computer Engineering, University of Central Florida, Orlando, FL 32816, USA*
[3] *Independent Researcher, Iran*
[4] *IMEC, Kissimmee, FL 34744, USA*
[*] *fathpour@creol.ucf.edu*

Abstract: Achieving ultrahigh-speed electro-optic modulators (subterahertz modulation bandwidths) is shown to be feasible in the thin-film lithium niobate integrated photonic platform. Design guidelines for optimization of the main radio-frequency and optical parameters are presented, and 3-dB modulation bandwidth up to 400 GHz is proved attainable in 3-mm-long devices. Such unprecedented bandwidths pave the path towards utilizing the devices in advanced optical communication systems.

1. Introduction

High-performance optical modulation is an essential part of modern communication systems. Ultrahigh-speed modulators are of great interest for ever-increasing aggregate bandwidth requirements of optical communication systems. Due to increased complexity of the electronic and photonic systems, reduction in power consumption, manufacturing cost, device footprint, and overall packaged size are also demanded for analog and digital applications [1–3]. Among platform candidates, Mach-Zehnder (MZ) modulators, operating based on the linear electrooptic (EO) or Pockel's effect, have been demonstrated to be superior, boasting up to ~100 GHz modulation bandwidth (BW), as well as > 20 dB extinction ratios [4,5]. Indeed, lithium niobate ($LiNbO_3$, LN) has been the standard material for the EO modulators (EOM) used in long-haul optical networks, due to its large EO coefficient (r_{33} = 31 pm/V) and fabrication maturity [4]. However, conventional LN waveguides (formed by in-diffusion of dopants or proton exchange processes) are bulky, i.e., their low index-contrast (< 0.1) yields weak optical confinement. As a result, high bending loss, long MZ electrode lengths, and low power efficiency due to large half-wave voltage-length product ($V_\pi.L$), render the EOMs unattractive for large-scale integration demands of advanced optical networks [4,5].

Thin-film approaches have been alternatively pursued to overcome these drawbacks of conventional LN devices and achieve ultracompact (submicron-scale) devices [6]. Particularly, exploiting heterogeneous integration techniques led to the emergence of ultracompact EOMs on silicon (Si) substrates [7]. This technology is potentially compatible with silicon photonics due to the choice of Si substrate. In order to attain lateral optical confinement and form submicron 2-D waveguides, one method is to rib-load the LN thin films with a refractive-index-matched material [7–9]. By utilizing the rib-loading method, difficulties of directly etching LN are avoided. However, it should be noted that, more recently, promising works have been reported on direct-etched LN thin films [10–12]. At any rate, high-speed thin-film LN EOMs with 3-dB BWs of 33 GHz and an extinction ratio of 18 dB have been reported on Si substrates [9]. Also recently, thin-film LN MZ EOMs with 3-dB BWs up to ~100 GHz have been demonstrated [13,14].

With this stage of maturity, accurate design of the ultracompact EOMs and reliable prediction

#355484 https://doi.org/10.1364/OE.27.006495
Journal © 2019 Received 19 Dec 2018; revised 23 Jan 2019; accepted 16 Feb 2019; published 20 Feb 2019

Optics EXPRESS

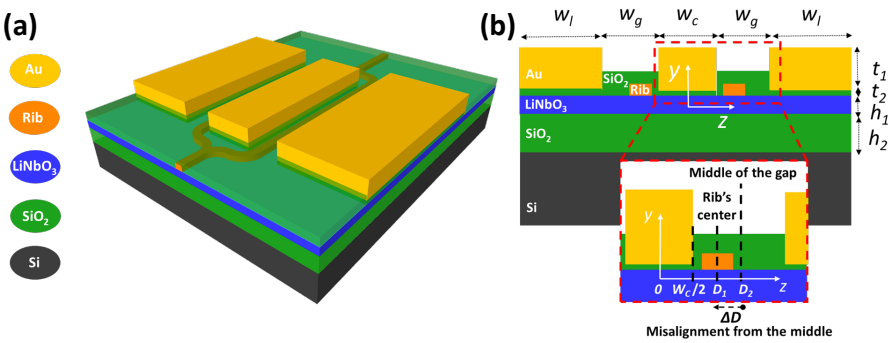

Fig. 1. (a) 3-D schematic of the thin-film LN MZ EOMs; (b) Cross-section of the EOMs in the lateral y-z plane. The zoomed section shows the misalignment ($\Delta D = D_2 - D_1$) of the rib's center (D_1) from the middle of the gap between the electrodes (D_2).

of their high-speed performance limits demanded an elaborate model. We have recently reported on such a general transmission-line model [15] and verified its accuracy by comparing the simulated results with prior experimental data [9].

In this work, novel designs are investigated in order to attain ultrahigh-BW (up to 400 GHz) MZ EOMs. Radio-frequency (RF) and optical parameters of the devices have been studied, and design guidelines and optimization procedures are presented for such unprecedented 3-dB modulation BWs for both rib-loaded and direct-etched thin-film LN EOMs. The present work paves the path towards exploiting the ultracompact devices in advanced integrated photonic circuits targeting futuristic optical communication applications, analog or digital, where subterahertz (sub-THz) BWs are desired. It is finally noted that optically-assisted characterization of EOMs in the sub-THz range is feasible [16]. However, full realization of functioning analog or digital communication systems will require development of ultrahigh-speed electronic and photodetection components, which are obviously beyond the scope of this work.

2. Design optimization

The 3-D schematic of the thin-film LN MZ EOM in the push-pull configuration is depicted in Fig. 1(a). The slab region of the optical waveguide is an X- or Y-cut LN thin film bonded to a thick SiO_2 buffer layer on a Si substrate. The thin film can be prepared through ion-implantation, wafer bonding, and thermal slicing processes [6,7]. The applied radio-frequency (RF) field, via the gold (Au) electrodes, is aligned along the Z-axis of the LN, in order to efficiently utilize the strongest EO coefficient of LN crystal (r_{33}). The thin-film LN is rib-loaded with a refractive-index-matched material, silicon nitride (SiN) for example [9], in order to provide lateral confinement for the optical mode. As mentioned, this method circumvents the need for direct etching of LN. However, it is important to note that the present work is not limited to rib-loaded waveguides. Designs for both optical waveguide platforms, i.e., rib-loaded LN and direct-etched LN (all-LN), are investigated and the results, along with the discussion on pros and cons of each method, are presented at the end of Section 2.

By using ANSYS HFSS and COMSOL commercial simulators, the main parameters of the EOM are investigated in order to optimize the structure for ultrahigh BWs. The three main parameters are the RF loss, the effective index mismatch between the RF and optical guided modes ($\Delta n = |n_{RF} - n_{op}|$), and the characteristic impedance of the electrodes (Z_0). Simulation results suggest that the key parameters that play an important role in defining the RF properties of the device are the thickness of the electrodes (t_2), the gap between the electrodes (w_g), and the middle electrode's width (w_c). As evident in Figs. 2(a) and 2(b), by increasing t_2, w_g, and w_c,

Optics EXPRESS

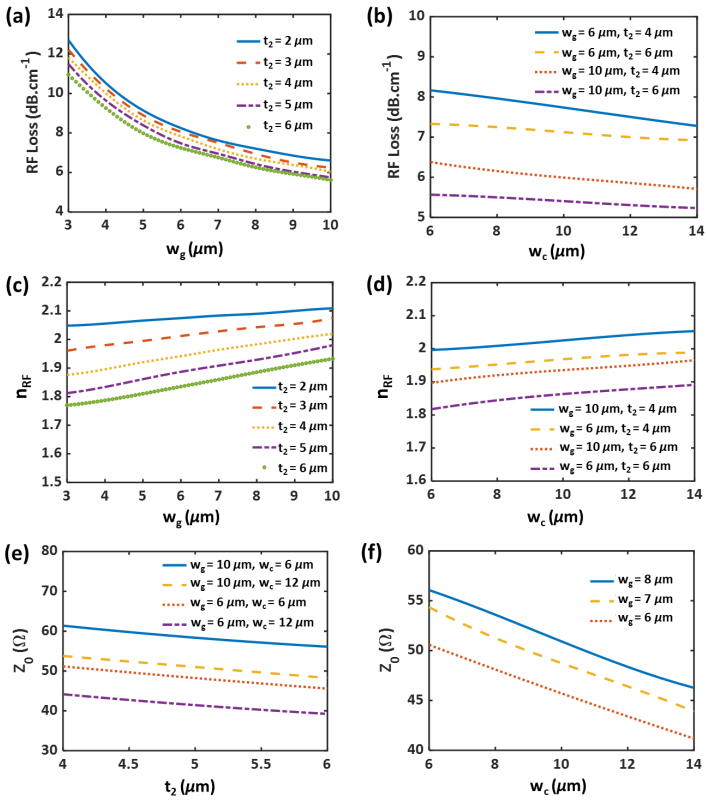

Fig. 2. RF design considerations (all performed at 100 GHz for w_l = 12.0 μm (w_c = 8.0 μm for (a), (c), and (e))): Variation of (a) RF loss vs. w_g for different values of t_2; (b) RF loss vs. w_c for different values of w_g and t_2; (c) n_{RF} vs. w_g for different values of t_2; (d) n_{RF} vs. w_c for different values of w_g and t_2; (e) Z_0 vs. t_2 for different values of w_g and w_c; and (f) Z_0 vs. w_c for different values of w_g.

RF loss decreases, and hence the final BW of the device is enhanced.

Another important parameter for BW enhancement is Δn. As n_{op} is constant within the concerned RF frequency (see Section 3 for example values), only the variations of n_{RF} versus t_2, w_g, and w_c are presented in Figs. 2(c) and 2(d). Depending on the optical waveguide structure and its calculated invariant n_{op}, n_{RF} can be appropriately tuned in order to minimize Δn.

It is well-known that Z_0 should be kept as close as possible to the 50-Ω terminating resistive load in order to reduce the impedance mismatch. The results for variation of Z_0, depicted in Figs. 2(e) and 2(f), suggest that this goal is achievable by varying the device dimensions for a specific RF frequency (e.g., 100 GHz in this case). However, as discussed later in Section 3, the frequency-dependence of Z_0 must be also considered in the overall design.

As the results in Fig. 2 imply, a larger w_g overall provides a more optimized design in terms of the RF loss. However, this increases $V_\pi.L$, and consequently lowers the power efficiency of the EOM. Meanwhile, as is evident in Figs. 3(a) and 3(b), the magnitude of the applied RF field is much larger at the edges of the middle electrode. In order to compensate for the increase in $V_\pi.L$, a solution is to place the optical waveguides closer to the middle electrode, instead of positioning them at the center of the gap between the electrodes, as is common practice. This has been studied in bulk LN devices in the past [17, 18] and is applied to thin-film devices here. As depicted in Fig. 4 for both rib-loaded and all-LN structures, employing this asymmetric

Optics EXPRESS

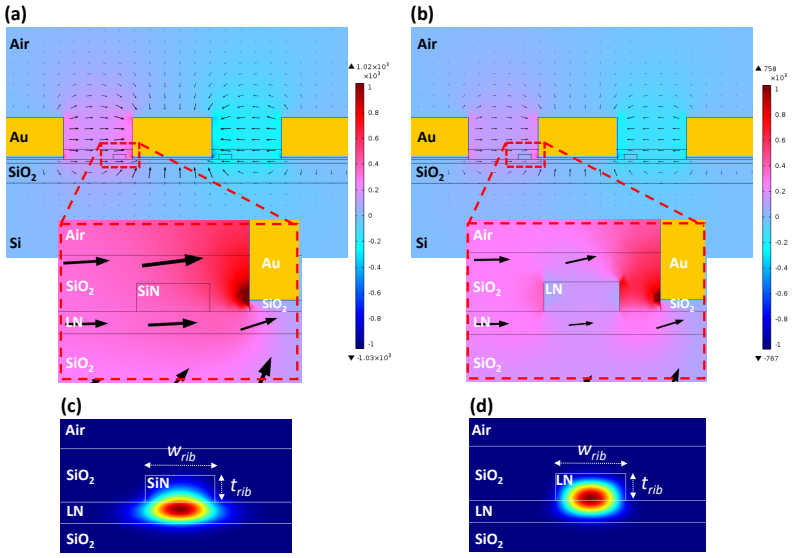

Fig. 3. Simulated RF mode profile for (a) rib-loaded and (b) all-LN EOMs with identical dimensions. Arrows are proportional to the magnitude of the field. Identical plot settings have been employed for COMSOL plots in both cases. Simulated TE optical mode profile for (c) rib-loaded and (d) all-LN waveguides with the same w_{rib} = 1.3 μm, t_{rib} = 0.5 μm, and a 1-μm-thick top cladding SiO_2 layer.

placement (see the inset of Fig. 1(b)) increases the overlap of the RF and optical field (Γ), while $V_\pi.L$ decreases accordingly, for any chosen value of w_g. As an example, for fixed w_c and w_g (both equal to 8.0 μm) and D_1 = 6.0 μm in Fig. 1, corresponding to $\Delta D = D_2 - D_1 = +2$ μm (instead of placing the waveguide in the center of the gap between the electrodes, giving $\Delta D = 0$), Γ increases by ~17% and ~19%, for rib-loaded and all-LN devices, respectively.

However, by moving the optical waveguides closer to the middle electrode, the metal-induced optical loss can increase significantly. This issue can be addressed by adding a thin SiO_2 buffer layer between the electrodes and the LN thin film, as schematically shown in Figs. 1 and 3. This decreases the additional loss dramatically, making it negligible, as depicted in Fig. 5. Specifically, for w_g = 7.0 μm (D_2 = 7.5μm), adding a 200-nm-thick buffer layer reduces the optical loss from ~100 to 0.1, and from ~1 to 0.001, all in dB/cm, for ΔD values of +2.0 μm and +0.5 μm, respectively.

Here, the pros and cons of rib-loaded versus all-LN designs are discussed. As first reported in [6, 15], and reconfirmed here in Figs. 3(a) and 3(b), the magnitude of the RF field in the LN region is relatively larger in the rib-loaded case compared to the all-LN case, due to the lower dielectric constant of SiN (~ 4) compared to LN (~ 40). This can be simply explained through the electromagnetic boundary conditions, i.e., the continuity of the normal component of the electric displacement field leads to a higher electric field in the medium with the lower dielectric constant. To attain high Γ, this advantage of the rib-loaded case is partially counteracted by its lower optical confinement. The transverse-electric (TE) optical mode profiles for both waveguides are presented in Figs. 3(c) and 3(d). Although ~65% of the optical mode is confined in the thin-film LN for the rib-loaded structure, the optical mode overlap with the LN region is higher (~95%) in the all-LN waveguide. This might allow for smaller gaps (w_g) between the electrodes in the all-LN EOM case compared to the rib-loaded counterpart, the issue of higher RF loss notwithstanding (see Fig. 2(a)). However, while the all-LN design can provide this stronger optical confinement and potential for smaller w_g, the aforementioned drop of the RF field in this

Optics EXPRESS

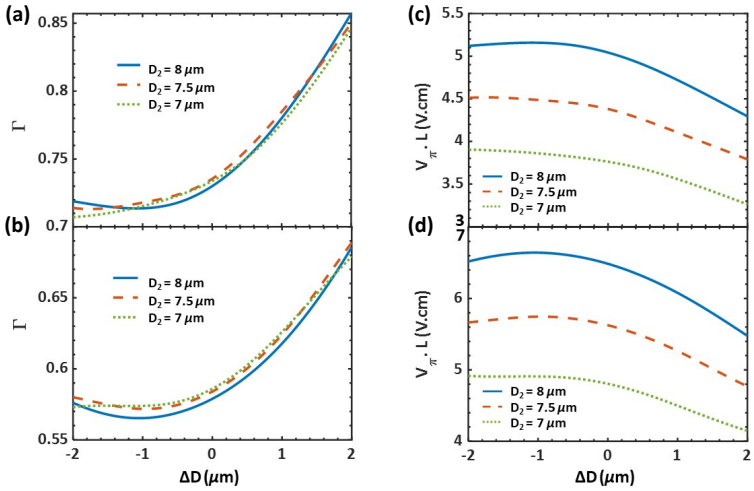

Fig. 4. Γ for (a) rib-loaded; (b) all-LN EOMs; $V_\pi.L$ for (c) rib-loaded; (d) all-LN EOMs, vs. ΔD (see Fig. 1(b)).

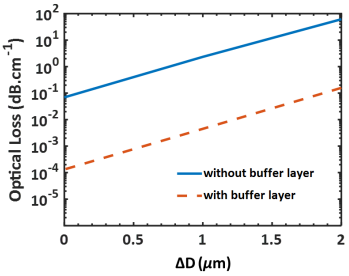

Fig. 5. Metal-induced optical propagation loss vs. ΔD (see Fig. 1(b)) for D_2 = 7.5 μm.

case leads to a smaller Γ and a higher $V_\pi.L$ compared to the rib-loaded device, for the same w_g and hence low RF loss. As an example, for w_g = 7.0 μm (D_2 = 7.5 μm) and ΔD = +2.0 μm, the rib-loaded design provides Γ = 0.825, which is 25% larger than that of all-LN design (Γ = 0.65), with corresponding $V_\pi.L$ values of 3.7 and 4.9 V.cm, respectively.

3. Final results and discussions

Based on the design considerations in Section 2, the final optimized design for the dimensions shown in Fig. 1 are summarized in Table 1. The optical waveguide dimensions w_{rib} and t_{rib} (defined in Fig. 3) are 1.3 and 0.5 μm for the rib-loaded, and 1.0 and 0.4 μm for the all-LN EOM, respectively. Different dimensions are chosen for the optical waveguide of each structure in order to minimize Δn and maximize Γ for both cases. The former helps to achieve the maximum possible final BW, while the latter improves the power efficiency of the device by reducing $V_\pi.L$.

Variations of different device metrics versus RF frequency are presented in Fig. 6. It is evident that n_{RF} drops sharply in the sub-GHz region, but remains fairly close to n_{op}, i.e., 1.91 and 1.96 for the rib-loaded and all-LN EOM, respectively, up to sub-THz frequencies, thus Δn remains small. As shown in Fig. 6(b), the RF loss of the optimized design is kept < 18 dB/cm up to 400 GHz, while Z_0 is kept close to 50 Ω for most of the frequency range.

Finally, by exploiting Eqn. (20) in [15], for the optimized design parameters presented in Table 1, the EO frequency responses of the rib-loaded as well as all-LN EOMs are summarized in

Optics EXPRESS

Table 1. Values of the geometrical dimensions in Fig. 1(b) for the optimized EOMs.

Parameter	w_l	w_g	ΔD	w_c	t_1	t_2	h_1	h_2
Value (μm)	12.0	7.0	2.0	8.0	0.2	4.0	0.4	2.0

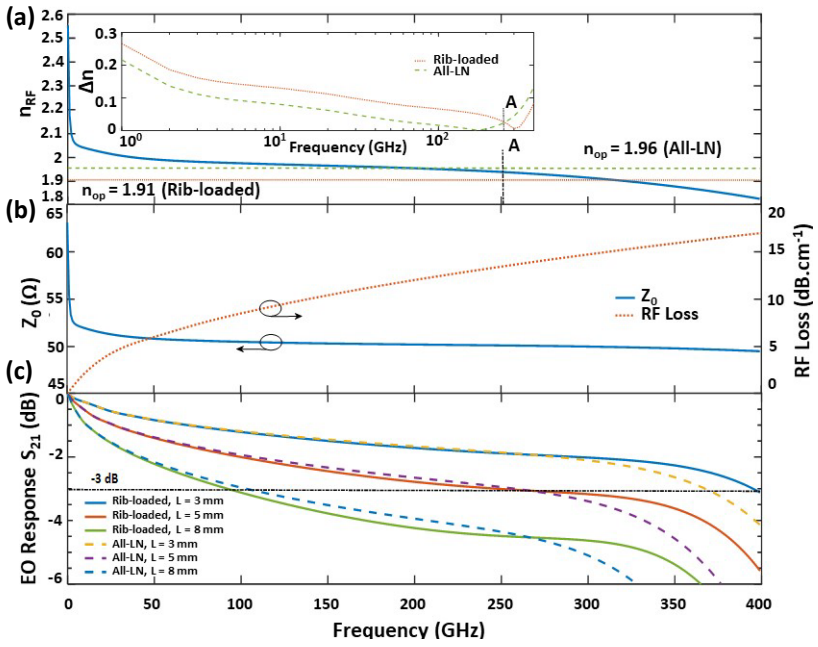

Fig. 6. (a) n_{RF}; (b) Z_0 and RF loss; (c) EO response (S_{21}) of the EOMs for different lengths. The horizontal dashed line shows the 3-dB electrical BW, and the inset depicts Δn.

Fig. 6(c) for three different electrode lengths, L. It is clear that shorter electrode lengths provide a larger 3-dB BW at the expense of increased V_π. The results predict that if sub-THz applications are desired and high voltages can be afforded (see Figs. 4(c) and 4(d)), an impressively high 3-dB BW of 395 and 368 GHz with corresponding V_π values of 12.3 V and 16.3 V can be attained for the rib-loaded and all-LN EOM cases, respectively, both with L = 3 mm. For L = 5 mm, a BW of ~250 GHz is exhibited which is 2.5 times larger than what is reported in [13, 14] for the same length and with comparable $V_\pi.L$. A comparison between rib-loaded and all-LN design for a fixed drive voltage is given in Table 2.

The higher BW in the rib-loaded design is worthy of discussion. The comparison between Δn of the rib-loaded versus all-LN EOM is depicted in the inset of Fig. 6(a). As the frequency is increased, the RF field concentration shifts more towards lower index materials (SiO_2 and air), and therefore the effective permittivity of the field decreases. As the figure implies, n_{RF} is virtually identical in both cases, while they possess different n_{op} values. Up to ~250 GHz, marked with an "A," n_{RF} remains close to the value of n_{op} in the all-LN design, and thus provides a slightly larger 3-dB BW compared to the rib-loaded counterpart. However, n_{RF} drops from ~1.95 at 250 GHz to ~1.83 at 400 GHz. Hence, in this region, Δn is smaller for the rib-loaded EOM which results in a larger BW.

In principle, choosing another rib-loading material with a different optical index and optimizing the RF and optical properties of the corresponding structure could lead to even higher BWs for the same L. In other words, the ~400 GHz given here for L = 3 mm is not necessarily the ultimate BW attainable in thin-film LN EOMs.

Optics EXPRESS

Table 2. Comparison between rib-loaded and all-LN design for a fixed drive voltage.

Drive Voltage (V)	*L* (cm)		BW (GHz)	
	Rib-loaded	All-LN	Rib-loaded	All-LN
1	3.7	4.9	5	3
5	0.74	0.98	110	66
10	0.37	0.49	362	256
15	0.24	0.32	420	340

4. Conclusion

We report on a novel design for ultracompact thin-film LN EOMs on Si substrates capable of operating up to ~400 GHz 3-dB modulation bandwidths for 3-mm-long MZ arms. Detailed design guidelines and optimization procedures for such an impressive performance are presented for future subterahertz optical communication system applications.

References

1. J. Yao, "Microwave photonics," IEEE J. Lightwave Technol. **27**(3), 314–335 (2009).
2. J. Capmany and D. Novak, "Microwave photonics combines two worlds," Nat. Photon. **1**, 319–330 (2007).
3. J. Yu, X. Li, and W. Zhou, "Tutorial: Broadband fiber-wireless integration for 5G+ communication," APL Phot. **3**(11), 111101 (2018).
4. E. L. Wooten, K. M. Kissa, A. Yi-Yan, E. J. Murphy, D. A. Lafaw, P. F. Hallemeier, D. Maack, D. V. Attanasio, D. J. Fritz, G. J. McBrien, and D. E. Bossi, "A review of lithium niobate modulators for fiber-optic communications systems," IEEE J. Quant. Elec. **6**(1), 69–82 (2000).
5. K. Noguchi, O. Mitomi, and H. Miyazawa, "Millimeter-wave Ti:$LiNbO_3$ optical modulators," IEEE J. Lightwave Technol. **16**(4), 615–619 (1998).
6. A. Rao and S. Fathpour, "Compact lithium niobate electrooptic modulators," IEEE J. Sel. Top. Quantum Electron. **24**(4), 1–14 (2018).
7. P. Rabiei, J. Ma, S. Khan, J. Chiles, and S. Fathpour, "Heterogeneous lithium niobate photonics on silicon substrates," Opt. Express **21**(21), 25573–25581 (2013).
8. A. Rao, A. Patil, J. Chiles, M. Malinowski, S. Novak, K. Richardson, P. Rabiei, and S. Fathpour, "Heterogeneous microring and Mach-Zehnder modulators based on lithium niobate and chalcogenide glasses on silicon," Opt. Express **23**(17), 22746–22752 (2015).
9. A. Rao, A. Patil, P. Rabiei, A. Honardoost, R. DeSalvo, A. Paolella, and S. Fathpour, "High-performance and linear thin-film lithium niobate Mach-Zehnder modulators on silicon up to 50 GHz," Opt. Lett. **41**(24), 5700–5703 (2016).
10. I. Krasnokutska, J. Tambasco, X. Li, and A. Peruzzo, "Ultra-low loss photonic circuits in lithium niobate on insulator," Opt. Express **26**(2), 897–904 (2018).
11. M. Zhang, C. Wang, R. Cheng, A. Shams-Ansari, and M. Loncar, "Monolithic ultra-high-Q lithium niobate microring resonator," Optica **4**(12), 1536–1537 (2018).
12. A. Rao, K. Abdelsalam, T. Sjaardema, G. F. Camacho Gonzalez, A. Honardoost, and S. Fathpour, "Highly efficient nonlinear integrated photonics in ultracompact periodically-poled lithium niobate on silicon," in *Frontiers in Optics* (Optical Society of America, 2018), paper JTu3A.59.
13. P. O. Weigel, J. Zhao, K. Fang, H. Al-Rubaye, D. Trotter, D. Hood, J. Mudrick, C. Dallo, A. T. Pomerene, A. L. Starbuck, C. T. DeRose, A. L. Lentine, G. Rebeiz, and S. Mookherjea, "Bonded thin film lithium niobate modulator on a silicon photonics platform exceeding 100 GHz 3-dB electrical modulation bandwidth," Opt. Express **26**(18), 23728–23739 (2018).
14. C. Wang, M. Zhang, X. Chen, M. Bertrand, A. Shams-Ansari, S. Chandrasekhar, P. Winzer, and M. Loncar, "Integrated lithium niobate electro-optic modulators operating at CMOS-compatible voltages," Nature **562**, 101–104 (2018).
15. A. Honardoost, R. Safian, A. Rao, and S. Fathpour, "High-speed modeling of ultracompact electrooptic modulators," IEEE J. Lightwave Technol. **36**(24), 5893–5902 (2018).
16. A. J. Mercante, S. Shi, P. Yao, L. Xie, R. M. Weikle, and D. W. Prather, "Thin film lithium niobate electro-optic modulator with terahertz operating bandwidth," Opt. Express **26**(11), 14810–14816 (2018).
17. R. A. Becker, and B. E. Kincaid, "Improved electrooptic efficiency in guided-wave modulators," IEEE J. Lightwave Technol. **11**(12), 2076–2079 (1993).
18. S. -J. Chang, C. -L. Tsi, Y. -B. Lin, J. -F. Liu, and W. -S. Wang, "Improved electrooptic modulator with ridge structure in X-cut $LiNbO_3$," IEEE J. Lightwave Technol. **17**(5), 843–847 (1999).